Chapter 5

Site-substitution effect on skyrmion phases of Cu_2OSeO_3

5.1 Introduction

The magnetic skyrmion lattices are a new state of matter with swirling spin, which protected from external perturbation through an intrinsic topological potential barrier [70]. This prevents skyrmion lattices from thermal fluctuation so that spin structure can remain intact. The energy barrier that established from the discontinuity to transmute between spin structures with topological charges n, which count the spin swirl around a unit sphere. n = 1 results in the skyrmion lattice and n = 0 results in the other noncollinear spin structure such as conical, spin helix and other complex collinear spin states orderings [9, 70, 153]. The discovery has mainly driven by the extensive investigation of skyrmion since they proposed to drive by ultra-low spin polarized current [137], turning magnetic skyrmion as a potential candidate for energy-efficient magnetic memory and other spintronic devices.

For a chiral spin system, the broken inversion symmetry stabilizes an asymmetric exchange interaction (Dzyaloshinskii-Moriya (DM)) that enforces a canted arrangement to the adjacent neighbouring spins [9, 154–156]. These competing interactions results in a non-colinear spin arrangement that responsible for stabilizing the trivial spin systems such as cycloid and helical spin orderings.

In a skyrmion lattice, the competition between the exchange interaction (J) and the asymmetric DM interaction (D) is a key factor that governs the formation and stablization of skyrmion lattices. The local exchange energy $\boldsymbol{E}_{ij}$ for such system is expressed as-

$$\boldsymbol{E}_{ij} = \sum_{<i,j>} -J_{ij} S_i \cdot S_j + D_{ij} \cdot S_i \times S_j \tag{5.1}$$

where S_i and S_j are the neighbouring spin sites, and D=|D|. The length scale of an isolated stable skyrmion is estimated by ratio (J/D) [157]. The stability of the skyrmion relies on the size of the skyrmion and the system size (L). For a chiral spin system, the skyrmion lattices are stabilized in the absence of an external magnetic field for L>(J/D)·a_{mag}, where a_{mag} is the magnetic lattice periodicity. However, for (J/D)· a_{mag} = L, the ground state could be degenerate with ferrimagnetic state and/or skyrmionics state [157, 158]. In the presence of any thermal perturbation, a critical values of magnetic anisotropies magnetic frustration, the magnetic skyrmion lattice is energetically favoured and a skyrmion phase in a plane perpendicular to the direction of an applied magnetic field can develop [159].

The skyrmion phase has been manifested in the intermetallic alloy Co-Zn-Mn [160, 161], thin film and bulk MnSi [162, 163], and bulk Cu_2OSeO_3 [164, 165] that offer unique opportunity to extend the investigation of these materials. One popular strategy to discover new helical spin system is redefining the non-centrosymmetric crystal lattices that have been well-known skyrmion host systems. Even after a decade of intensive investigations, skyrmion-hosting materials remain notable small in number. Specific structural properties such as the lack of inversion symmetry and magnetic features like ferromagnetism and the presence of DM interactions is essential to establish the evolution of magnetic skyrmion [9, 70, 153]. The popular means to enhance the number of host materials is chemical doping in well-known canonical skyrmion-hosting systems. This method has been already examined for Cu_2OSeO_3 skyrmion lattice by substituting Cu with Zn and Ni that generate significant modifications in intrinsic skyrmion phases [82, 166].

Generally, the Mott insulator Cu_2OSeO_3 crystallizes in non-centrosymmetric $P2_13$ space group. Two Cu^{2+} cations in trigonal bipyramidal (CuI) and square pyramidal (CuII) coordination geometry are present that responsible for the formation of ferrimagnetic lattice [71, 167, 168]. The magnetic exchange interactions between spins are interlinked by oxygen atoms via super-exchange interactions [169, 170]. It has been reported that magnetic moment of Cu_2OSeO_3 monotonically decreases with increasing Zn-substitution levels [82]. This effect has been interpreted in terms of the site-specific substitution of Cu^{2+} cation at the CuII-site by a non-magnetic Zn^{2+}. Stefancic *et al.* [171] observed splitting of the skyrmion phase in $(Cu_{1-x}Zn_x)_2OSeO_3$ attributed to the multi-phase nature

of the polycrystalline skyrmion host materials. Sukhanov *et al.* [172] observed that Cu ions are replaced by either magnetic (nonmagnetic) within a critical limit of low impurity concentration in Cu_2OSeO_3 found that all the substituted compounds possess a helical spin structure in applied magnetic fields at temperatures near to T_C which was very identical to the pristine Cu_2OSeO_3 [82, 171, 172].

In this study, investigation of the Cd-doped Cu_2OSeO_3 nanocrystallites as host materials for magnetic skyrmion is conducted. The structural, electronic and magnetic properties of both Cd-doped and pristine Cu_2OSeO_3 were investigated. Experimental findings suggest that chemical substitution stabilized the magnetic skyrmion lattices.

5.2 Experimental details

Cd-doped Cu_2OSeO_3 crystallites were synthesised by the conventional solid-state reaction. Stoichiometric mixtures of CuO and SeO_2 precursor powders were ground manually and pressed in the form of pallets. The pallets were then sealed in an evacuated quartz tube. The reaction mixture took placed at elevated temperature 600 °C that was ramped up with a constant rate of 50 °C h^{-1} for 12 h. This thermal treatment followed by quenching of reaction tube in a water bath. This reaction results a greenish powder that mostly a mixed-phase compound. To obtain the undoped sample in pure phase, a routine heat-treatment with various intermediate stages for 15 days was conducted, as illustrated in Fig. 5.1(a). The olive-green colour single-crystalline nanocrystals of the undoped samples were obtained. Interestingly, with nominal Cd-doping followed by one step heat treatment for 12 h $(Cu_{1-x}Cd_x)_2OSeO_3$ (x = 0.02) were obtained. Finally, the resulting a dark greenish single phase nanocrystals (see Fig. 5.1(b)). Both doped and pristine samples were used for further various characterizations and analysis.

The crystal structure and phase purity identification of the samples were determined via X-ray diffraction (XRD) using a diffractometer (Rigaku, Mini Flex 300/600, Japan). Cu-K_α (λ = 1.5406 Å) was used as a probe source. The XRD patterns were refined with the FullProf Suite [173]. For the analysis, the diffraction patterns were recorded in the range of 10°–90° with a constant scan rate was 2° min^{-1} with a step size of 0.02°. Rietveld refinement of XRD patterns was consistent with single-phase cubic Cu_2OSeO_3 ($P2_13$). No other impurities phases were detected within the limit of experimental noise. The observed broad diffracted peaks were indicating the formation of nanosized crystallites of Cu_2OSeO_3. The average crystallite sizes of the samples were estimated using the Scherrer formula [27]. TEM (Tecnai G2 20 TWIN, USA) was used to study the microstructure and crystalline properties. Selected area electron diffraction (SAED) data were indexed

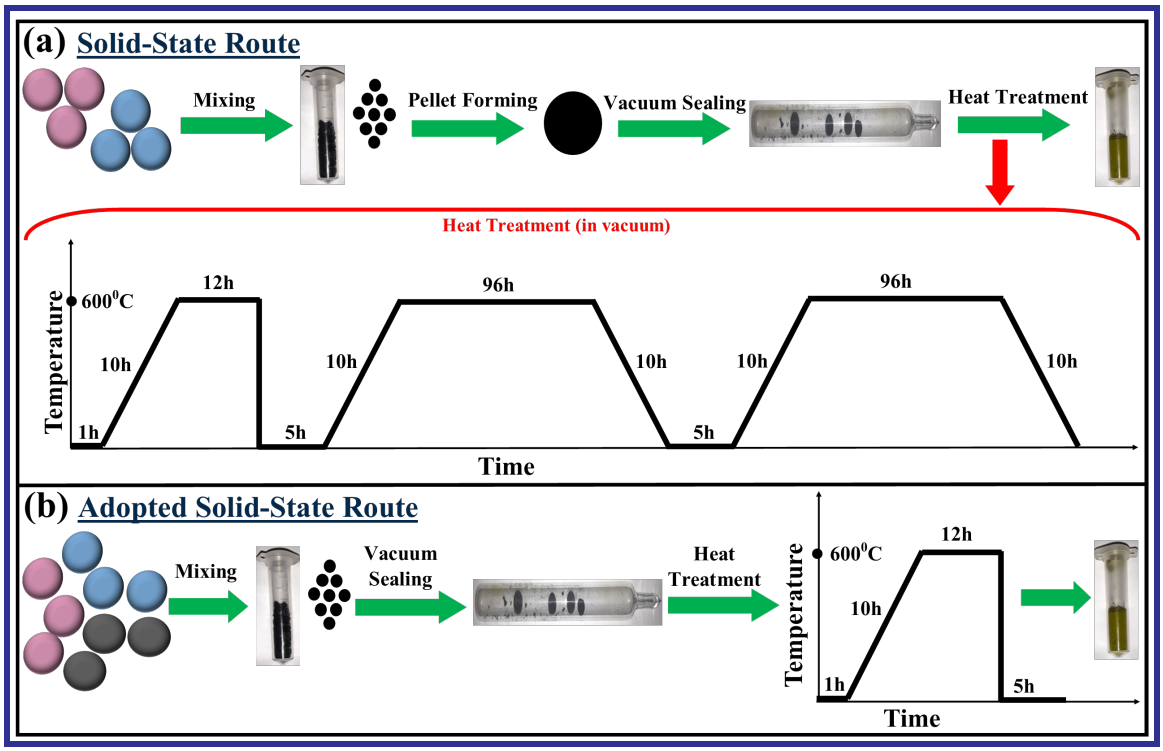

Fig. 5.1 Systematic for the synthesis of Cu_2OSeO_3 and $(Cu_{0.98}Cd_{0.02})_2OSeO_3$ nanocrystallites

by CrysTBox software [174]. Homogeneity and elemental compositions were analysed with the EDX. The oxidation states of the constituent elements and stoichiometry were investigated through X-ray photoelectron spectroscopy (XPS) measurements, which was performed on both doped and pristine samples. The survey XPS maps of Cu-2p, O-1s, and Se-3p were collected using Al-K_α. SQUID-VSM magnetometer (MPMS-3X, Quantum Design) was used to detect the effect of Cd-doping on temperature-dependent magnetic properties (M-T).

5.3 Results and discussions

5.3.1 Structural characterizations

Fig. 5.2(a) shows the XRD pattern of pristine and Cd-doped Cu_2OSeO_3 quenched sample at 600 °C represents the mixed-phase. The observed peak positions and diffraction patterns are in well agreement with the JCPDS database of Cu_2OSeO_3 powder sample. With rigorous heat-treatment processes of nearly 15 days undoped sample transform into a single phase that suggests a perfect matching with literature single phase as shown in Fig.

5.2(b). With nominal doping of Cd (2%) on Cu_2OSeO_3 followed by one step heat-treatment, alternatively, grown in a single-phase nono-crystalline sample. The XRD patterns of the both doped and undoped samples ensured that both of the samples possessing an identical crystal structure as depicted in Fig. 5.2(a).

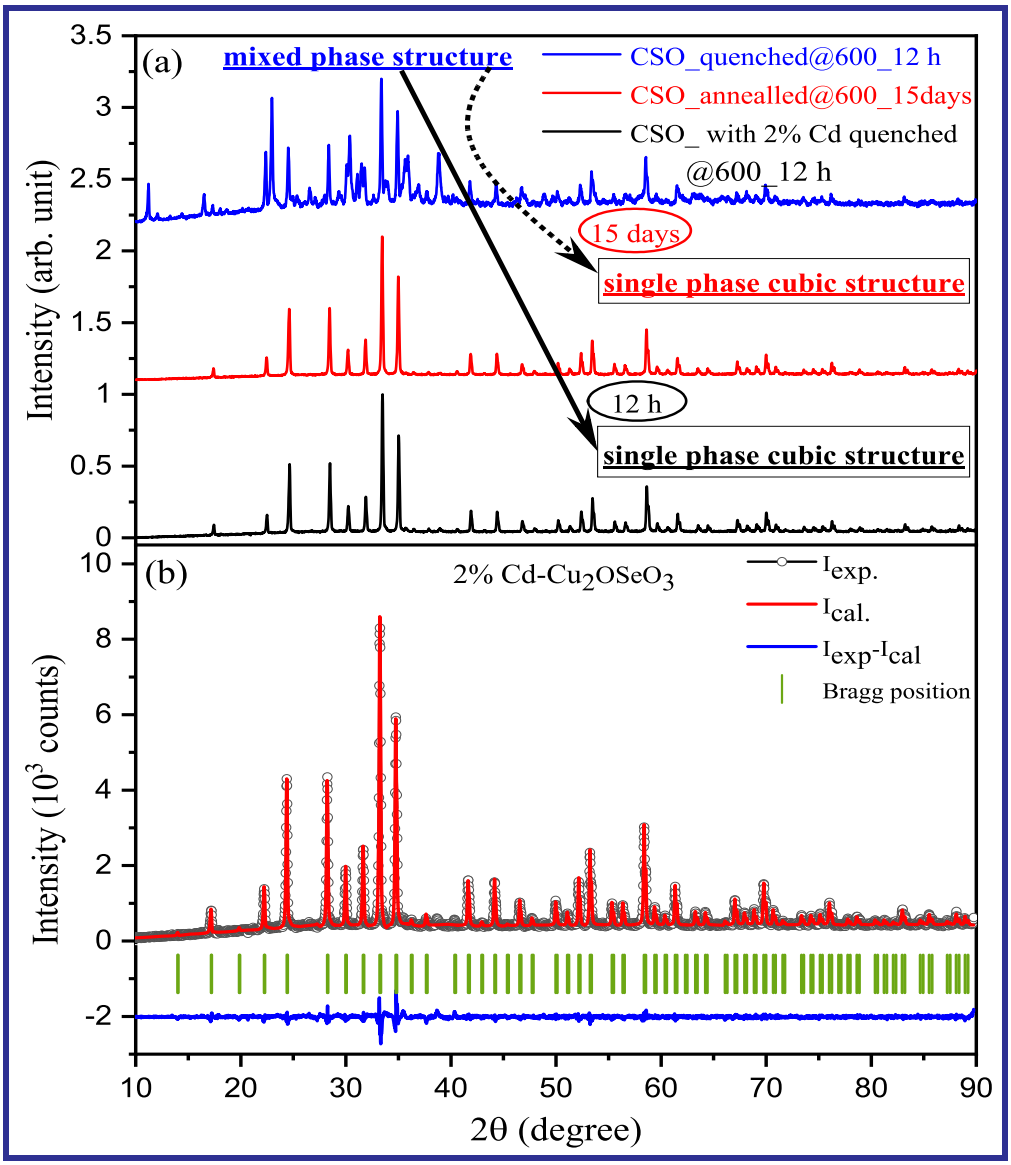

Fig. 5.2 XRD pattern evolution of the $(Cu_{0.98}Cd_{0.02})_2OSeO_3$ powder samples for various stages of heat-treatments from the mixed phase to single phase, and (b) single phase refined XRD pattern for $(Cu_{0.98}Cd_{0.02})_2OSeO_3$ sample.

A well indexed XRD patterns along with simulated XRD diffraction patterns are shown in Fig. 5.2(b). The background and peak shape fitted with linear interpolation and pseudo-Voigt function using Full Prof Software Suite [173]. Lattice parameters, scale factor, and

positional coordinates were varied to obtain the agreement factor with fitted parameters like R_p, R_{wp}, R_e and χ^2 are 18.5, 17.0, 10.6, and 2.55, respectively. Fig. 5.2(b) also depicts a relative comparison between the experimental (open black circles) and simulated (solid red line) XRD patterns, which are in good agreement as can be realized from the difference curve (blue bottom line). Most of the Bragg's reflections (vertical green bar) are in an excellent agreement with experimental patterns. The lattice parameters ($a = b = c$ = 8.9330(4) Å, and α=β=γ=90°) were used in well-matched with single-phase cubic structure having space group $P2_13$ (JCPDS database card No.: 000460793). The crystallite size (D) of both doped and undoped samples was calculated by estimating the full width at half maxima (FWHM) of the prominent and intense XRD peaks and applying the Scherrer formula [175]. The typical obtained value of D was ranging from 45 and 50 nm. Nominal doping of Cd (2%) can enhance the nucleation sites to the lattice system, as confirmed in Fig. 5.2(b). The quenching induces the residual stresses between Cu_2OSeO_3 matrices and the reinforced particles along with strain [176, 177].

Fig. 5.3 shows the TEM images and SAED pattern of $(Cu_{1-x}Cd_x)_2OSeO_3$ (x ≈ 0.2) nanocrystals. The elongated crystallites were clearly observed as shown in Fig. 5.3(a). The average size of these crystallites range over 50–200 nm. The TEM image of $(Cu_{1-x}Cd_x)_2OSeO_3$ (x ≈ 0.2) is depicted in Fig. 5.3(b). The lattice fringes indicate a high crystallinity of the Cu_2OSeO_3 nanocrystal with the inter-planar spacing (d) of 0.5035 nm corresponds to (1 1 1) plane. The obtained d value was comparable to estimated data from XRD patterns. Fig. 5.3(c) shows the SAED pattern that verifies the high crystallinity of the nanocrystal. The enlarged view of Fig. 5.3(c) shows the well-indexed SAED pattern and further confirmed the cubic crystal structure. The inter-planar spacings estimated from SAED patterns, shows a good agreement with XRD data.

The single-crystalline SAED patterns were reported with experimental results in poly crystalline Cu_2OSeO_3 powders, which is theoretical in well agreement for a cubic system and hold the d (inter-planer spacing) and R (distance between transmitted and diffracted beam) relation for a cubic system, $\frac{d_1}{d_2}=\frac{R_2}{R_1}=\frac{\sqrt{N_2}}{\sqrt{N_1}}$; $N \equiv h^2 + k^2 + l^2$. In contrast to Fig. 5.3(d), the angle between the planes ($\bar{1}$ 1 0) & ($\bar{3}$ 0 3), ($\bar{3}$ 0 3) & (($\bar{2}$ $\bar{1}$ 3), ($\bar{2}$ $\bar{1}$ 3) & ($\bar{1}$ $\bar{2}$ 3), ($\bar{1}$ $\bar{2}$ 3) & (1 $\bar{1}$ 0) are 60.15°, 19.23°, 21.86°, 78.76°, respectively, interpreted with the CrysTBox software [174]. The expression between angle and miller indices for cubic system is can be written as-

$$\cos(\theta) = \frac{h_1h_2 + k_1k_2 + l_1l_2}{\sqrt{(h_1^2 + k_1^2 + l_1^2)(h_2^2 + k_2^2 + l_2^2)}} \tag{5.2}$$

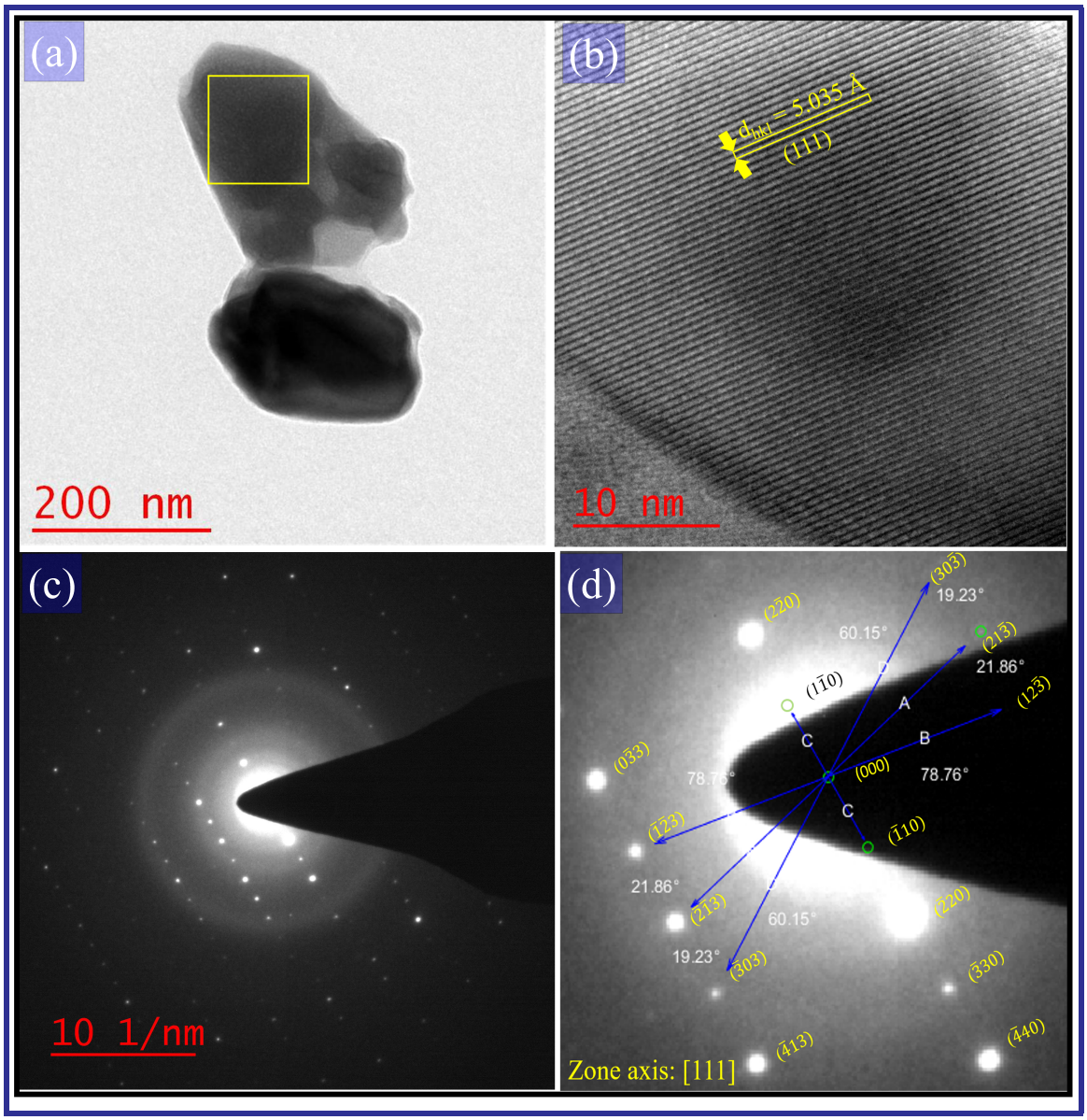

Fig. 5.3 (a) TEM image of Cd-substituted Cu_2OSeO_3 nanocrystals prepared by adopted solid-state route, HRTEM image (b) of individual Cd-substituted Cu_2OSeO_3 nanocrystals, and the corresponding SAED pattern (c) and enlarge and indexed pattern (d).

where θ is corresponding angle between $(h_1k_1l_1)$ & $(h_2k_2l_2)$ crystallographic planes. All angles between the different crystallographic planes measured from SAED pattern are in excellent agreement with angles estimated from Eq. 5.1. The crystallographic zone axis is estimated to be [111] that indicates single crystalline cubic Cu_2OSeO_3 nanocrystals growth direction and all indexed planes are correspond to the zone axis.

5.3.2 Compositional analysis of Cd-Cu_2OSeO_3

The elemental mapping and EDX spectra of Cd-doped Cu_2OSeO_3 are shown in Fig. 5.4. The scanned image of sample $(Cu_{0.98}Cd_{0.02})_2OSeO_3$ is shown in Fig. 5.4(a), and complete elemental scan of Cu-K, Cd-L, Se-K and O-K shown in Fig. 5.4(b). Individual mapping of

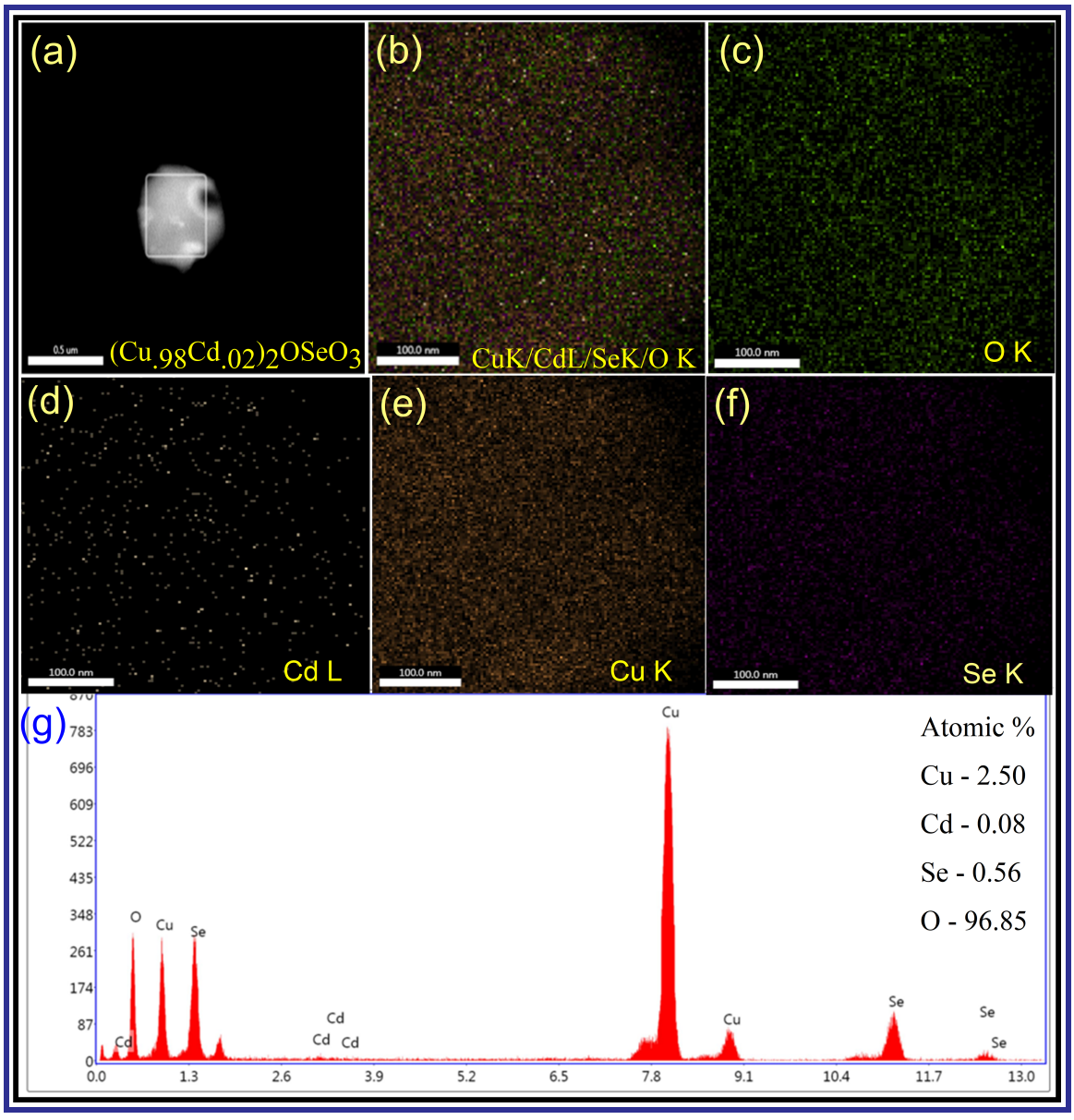

Fig. 5.4 Elemental mapping and EDX data. (a) Image of sample $(Cu_{0.98}Cd_{0.02})_2OSeO_3$ and (b) complete elemental scan of Cu, Cd, Se and O. (c)–(f) Individual mapping of elements present in $(Cu_{0.98}Cd_{0.02})_2OSeO_3$ and (g) EDS spectra for the present elements like Cu, Cd, Se, and O, equipped with transmission electron microscope.

elements (Cu, Cd, Se, and O) present in $(Cu_{0.98}Cd_{0.02})_2OSeO_3$ are distributed uniformly throughout the nanocrystallites as shown in Figs. 5.4(c-f). EDS spectra for the present elements like Cu, Cd, O, and Se represent the atomic fraction of elements (see Fig. 5.4(g)), which is in well agreement to that the doped Cu_2OSeO_3 revealing the excellent quality of nanocrystallites.

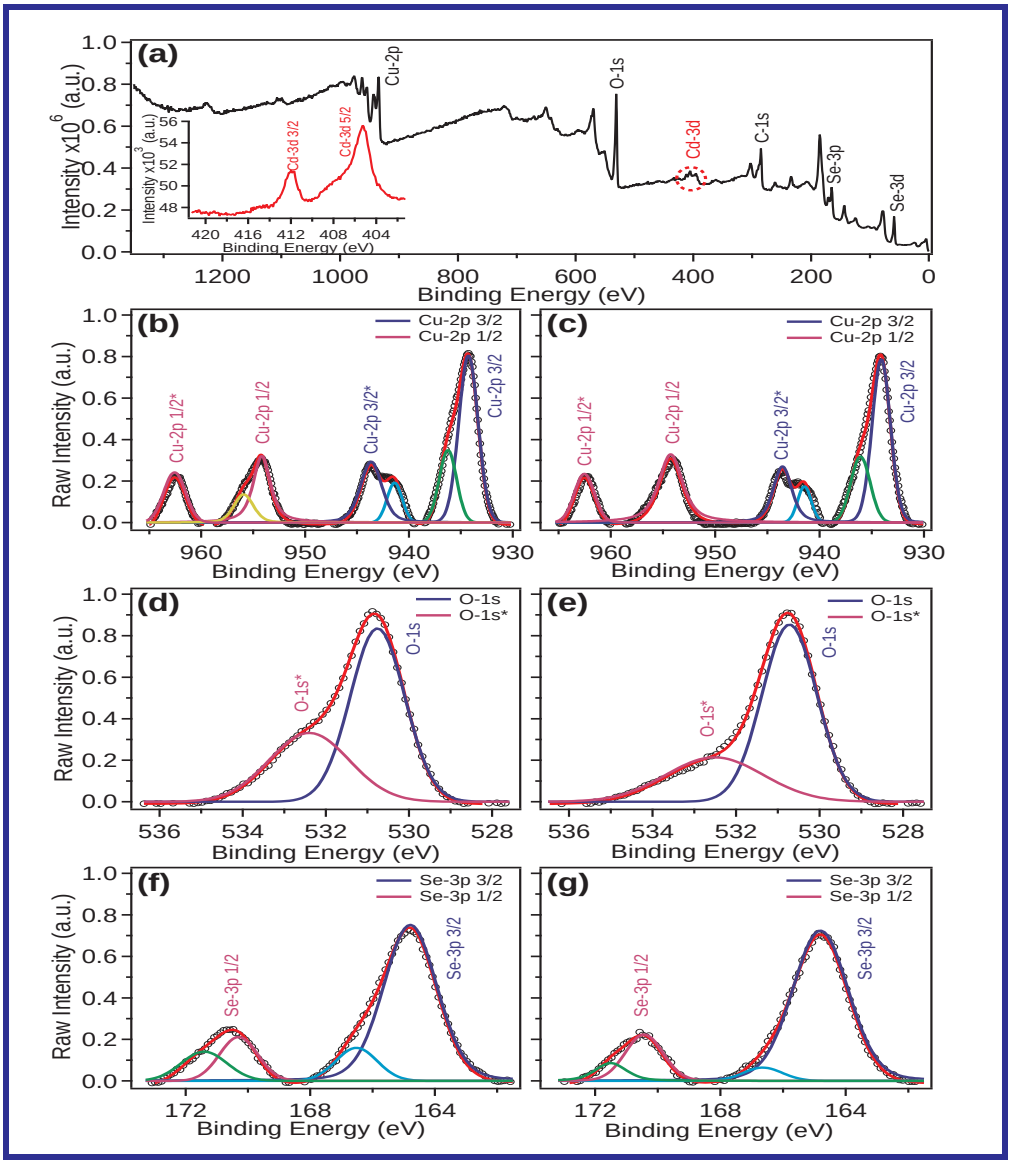

Fig. 5.5 (a) wide- survey XPS scan (b), (c) Cu-2p, (d), (e) O-1s, (f), (g) Se-3p for Cu_2OSeO_3 and $(Cu_{0.98}Cd_{0.02})_2OSeO_3$ nanocrystallites with fitted curves.

Table 5.1 XPS data fitting parameters for elements O, Cu, Se, and Cd for doped and undoped Cu_2OSeO_3

Serial No.	Index Peaks/Fitting parameters	Cu_2OSeO_3			Cd-Cu_2OSeO_3		
		B.E. (eV)	FWHM (eV)	Area (units)	B.E. (eV)	FWHM (eV)	Area (units)
1	C-1s	284.8	1.1	1.0	284.9	1.2	1.1
2	Cu-2p3/2	934.3	2.1	1.9	934.0	2.0	1.7
3	Cu-2p*3/2	934.6	2.4	0.8	943.5	2.1	0.7
4	Cu-2p1/2	954.1	1.9	0.9	954.2	2.7	1.2
5	Cu-2p*1/2	962.5	2.4	0.6	962.5	2.2	0.5
6	Se-3p3/2	164.7	2.0	1.7	164.8	2.1	1.7
7	Se-3p1/2	170.3	1.4	0.3	170.4	1.4	0.3
8	O-1s	530.7	1.5	1.3	530.7	1.5	1.4
9	O-1s*	532.4	2.2	0.7	532.5	2.7	0.6

5.3.3 Electronic properties of Cd-Cu_2OSeO_3

The valence states of the elements were probed by XPS spectra which were performed on the freshly prepared $(Cu_{0.98}Cd_{0.02})_2OSeO_3$. Wide XPS spectra of Cd-2p, Cu-2p, O-1s and Se-3p were collected using a non-monochromatic Al-K energy (E = 1487.6 eV) X-ray source and an electron-analyzer. Figs. 5.5(a-g) shows the XPS spectra of nanoparticles corresponding to Cd-2p, Cu-2p, O-1s, and Se-3p. The binding energies (BE) of elements were matched with C-1s (BE = 284.8 eV) peak. Cu-2p spectra (Figs. 5.5(b-c)) deconvoluted into different individual peaks for binding energies of 934.3 eV, 954.1 eV, 943.6 and 962.5 eV. The BE of the Cu-2p core level at 934.3 and 954.1 eV can be attributed to Cu-$2p_{3/2}$ and Cu-$2p_{1/2}$, respectively. Cu-$2p^*_{3/2}$ (BE = 943.5 eV) and Cu-$2p^*_{1/2}$ (962.5 eV) are the Cu-satellite peaks.

The Cu-2p satellite peaks are indicating the presence of Cu in 2+ valence state [178]. XPS spectra of O-1s (Figs. 5.5(d, e)) show peak at 530.7 eV that can be attributed to bulk O^{2-} of the cubic lattice system. Experimental data suggest an absence of any chemisorbed oxygen, indicating the excellent stoichiometry of Cu_2OSeO_3 nanoparticles. Figs. 5.5(f-g) shows the BE at 164.7 and 170.3 eV that correspond to Se-$3p_{3/2}$ and Se-$3p_{1/2}$ orbitals, respectively. These peaks represent the Se^{4+} valence state. The relative areas of Se-2p and Cu-2p suggest that Se to Cu atomic ratio of approximately 1:2 and indicate the stoichiometry of Cu_2OSeO_3 nanoparticles. Table 5.1 shows the details of fitted parameters like BE, FWHM, peaks area for both undoped and doped samples.

5.3.4 Magnetic properties of Cd-Cu_2OSeO_3

The temperature-dependent magnetization measurements were conducted in zero field cooled (ZFC) protocol with an applied field of 250 Oe for the doped and pristine samples are shown in Fig. 5.6. Curie temperature (T_C = 62.72(36)K) and Curie constant (C = 2.96×10^{-6}) of the quenched sample, which is well consistent with the reported data. For Cd-doped Cu_2OSeO_3, the ferrimagnetic transition temperature is almost insensitive to Cd concentration having a minimal variation in moments for nominal Cd doping.

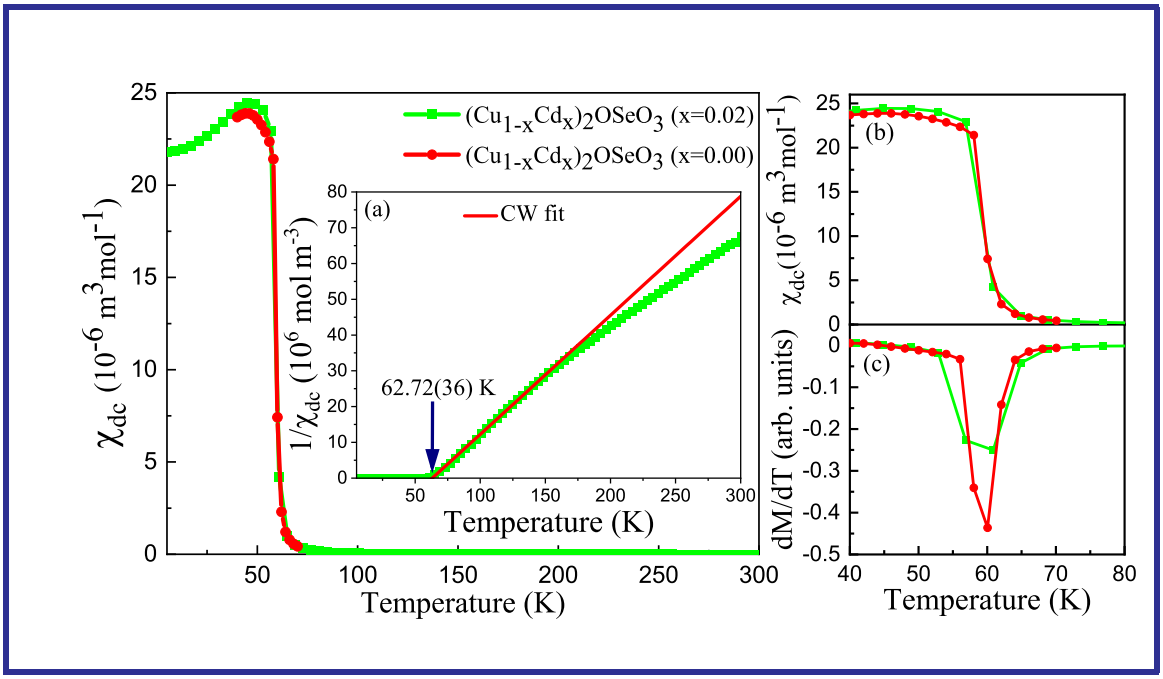

Fig. 5.6 Temperature-dependent magnetization of $(Cu_{1-x}Cd_x)_2OSeO_3$ (x $\approx$ 0.2) nanocrystals measured in ZFC protocol at 250 Oe. Inset Fig. (a) represents the ($1/\chi_{dc}$, T) magnetic susceptibility as a function of temperature. Fig. (b) and (c) represent the main magnetic transition and the variation of derivative of magnetization as a function of temperature for doped and undoped samples.

The inset Fig. 5.6(a) shows the ($1/\chi_{dc}$, T) magnetic susceptibility and revealing transition temperature of 62.72(36) K, which is same as reported in the bulk material. This suggests that this material is not only similar to the bulk state, but also exhibits the same phase. Despite, the nanocrystals of Cu_2OSeO_3 show the signature of a spin spiral at low temperature below 50 K that can be seen in Figs. 5.6(b, c). These findings are very significant because our analysis reveals that the present system also lacks the inversion symmetry, ensuring the emergence of DM interaction as in bulk Cu_2OSeO_3. Figs. 5.6(b, c) shows the variation of magnetization and its derivative as a function of temperature in the vicinity of skyrmion phase transition. A transition is appeared at 60 K shown in Fig. 5.6(c)

for both samples, which is the hallmark signature of materials hosting skyrmion lattice phases [81, 179].

5.4 Summary and conclusions

In summary, this chapter demonstrated a strategy for the fabrication of Cu_2OSeO_3 nanocrystallites by solid-state with a nominal Cd (2%) doping followed by one step heat-treatment for 12 h, which is faster than the reported route of sample prepared by solid-state, hydrothermal, and chemical route. The XRD patterns reveal Cu_2OSeO_3 phase was stabilized 10 times faster than the conventional solid-state route with a nominal fraction of Cd (2%) followed by one-step heat-treatment for 12 h. TEM data also supports the phase quality and excellent crystallinity of powder sample. The proposed method can result in the elongated Cu_2OSeO_3 nanocrystals (size 50–200 nm) with excellent crystallinity. These findings are essential steps forward the technological applications of magnetic skyrmion for designing the ultra-dense spintronics devices.